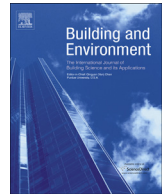Since January 2020 Elsevier has created a COVID-19 resource centre with free information in English and Mandarin on the novel coronavirus COVID-19. The COVID-19 resource centre is hosted on Elsevier Connect, the company's public news and information website.

Investigating the impact of gaspers on cabin air quality in commercial airliners with a hybrid turbulence model

Ruoyu You [a], Jun Chen [a], Chao-Hsin Lin [c], Daniel Wei [d], Qingyan Chen [a, b, *]

[a] School of Mechanical Engineering, Purdue University, West Lafayette, IN 47907, USA
[b] Tianjin Key Laboratory of Indoor Air Environmental Quality Control, School of Environmental Science and Engineering, Tianjin University, Tianjin 300072, China
[c] Environmental Control Systems, Boeing Commercial Airplanes, Everett, WA 98203, USA
[d] Boeing Research & Technology, Beijing 100027, China

ABSTRACT

It is not clear whether turning on the gaspers in the cabins of commercial airliners actually improves the air quality. To answer this question, this study first developed a hybrid turbulence model which was suitable for predicting the air distribution in an aircraft cabin with gaspers turned on. Next, the investigation validated the model using two sets of experimental data from a cabin mockup and an actual airplane. This study then used the validated model to systematically investigate the impact of gaspers on cabin air quality in a seven-row section of the fully-occupied, economy-class cabin of Boeing 767 and 737 airplanes. The CFD calculations formed a database consisting of 9660 data points that provide information about SARS infection risk. It was found that the distribution of opened gaspers can influence the infection risk for passengers. Even though the gasper supplies clean air, it is possible for it to have a negative impact on the passengers' health. Statistically speaking, the overall effect of turning on the gaspers on the mean infection risk for the general population was neutral.

© 2016 Elsevier Ltd. All rights reserved.

1. Introduction

In commercial airliners, a strong association has been observed between cabin airflow patterns and the transmission of airborne infectious diseases [1]. These diseases include influenza [2], tuberculosis [3], and severe acute respiratory syndrome (SARS) [4]. With the rapid increase in air travel [5], improving cabin air quality has become crucial to public health. In commercial airplanes, personalized ventilation is typically provided by a system of gaspers, the small, circular, and adjustable vents above the seats passengers. When passengers turn on the gaspers, the air distribution in the cabin is altered [6,7]. Consequently, the transport of airborne infectious contaminants is affected [8]. It is important to investigate the impact of gaspers on cabin air quality in commercial airliners in order to evaluate the effectiveness of gasper-induced ventilation in reducing the risk of infection.

A number of studies have measured the airflow distribution of a jet from a gasper. For example, Dai et al. [9] used a high-precision hotwire anemometer to measure the velocity magnitude and turbulence intensity in the flow field of a gasper-induced isothermal flow. They found that the flow field was complex near the nozzle but could be simplified as a round jet when the flow was fully developed. You et al. [6] measured the airflow field in a full-scale, half-row, single-aisle aircraft cabin mockup with one gasper turned on, using a particle image velocimetry (PIV) technique. The measured data showed that the gasper-induced flow, the main flow in the cabin, and the thermal plume from a passenger interacted with each other and formed a complex flow field. Li et al. [8] measured the distributions of air velocity, temperature, and contaminant concentrations in the economy cabin of a functional MD-82 airplane with gaspers on and off. Although the gaspers directed clean air toward the passengers, the cabin air quality in this case was not improved.

In addition to experimental studies, several investigations have focused on the modeling of a gasper-induced jet with computational fluid dynamics (CFD). For instance, You et al. [6] evaluated the performance of the renormalization group (RNG) k-ε model and the shear stress transport (SST) k-ω model using their measured data. The SST k-ω model was found to be more accurate than the

RNG k-ε model for predicting the air distribution of a gasper-induced jet. Shi et al. [10] calculated the entrainment ratio at different locations along a gasper-induced jet using a CFD model. They found that over 90% of the air in the breathing zone of a passenger was entrained from the surroundings when the gasper was turned on. Note that both of these studies used a detailed geometry with a large grid number to represent the actual gasper in the CFD simulations, which led to an unacceptably high computing cost. To overcome this problem, You et al. [7] developed a simplified gasper model to reduce the grid number for the gaspers without compromising the accuracy of the results.

Although the studies reviewed above have provided great insight into gasper-induced flow, there is a lack of systematic studies on the impact of gasper-induced ventilation on cabin air quality in commercial airliners. Namely, there is not a clear answer to the following question: will turning on the gaspers improve the cabin air quality in commercial airliners? To answer this question, this study first developed a hybrid turbulence model which was more suitable than previous models for predicting the air distribution in an aircraft cabin with gaspers turned on. The developed model was then validated using two sets of experimental data measured in a cabin mockup and an actual airplane. In addition, this investigation used the validated model to calculate the risk of infection by SARS in the seven-row section of economy-class cabin of two popular airplanes, Boeing 767 and 737, with different gasper on/off distributions. The database consisted of 9660 infection-risk data points, which were then used to explore the impact of gaspers on cabin air quality in the two airplanes.

2. Model development

To obtain the air distribution in an aircraft cabin with gaspers turned on, it is important to identify an accurate and robust turbulence model. According to a number of comparative studies, the RNG k-ε model is the most robust Reynolds-averaged Navier-Stokes (RANS) model for predicting air distribution in the bulk air regions in enclosed environments [11–14]. However, the RNG k-ε model fails to accurately predict the complex airflow in the near wall regions, because it uses a wall function instead of resolving the near wall airflow. In aircraft cabins, the airflow near a human body, where the gasper-induced jet encounters the thermal plume, could be very important in terms of thermal comfort and contaminant transport [6]. Several comparative studies found that the SST k-ω model was superior in predicting airflow in the near wall regions [6,10]. This is because the SST k-ω model uses the standard k-ω model in the near wall regions, which resolves the near wall airflow. In the bulk air regions, however, the SST k-ω model utilizes the standard k-ε model, which is less robust than the RNG k-ε model. Therefore, it is worthwhile to develop a hybrid turbulence model for cabin airflow simulations, one which will not only be robust in the bulk air regions but also accurate in the near wall regions. This hybrid turbulence model will use the standard k-ω model in the near wall regions and a transformed RNG k-ε model in the bulk air regions. A blending function will be employed to gradually switch the two models on and off. This section details the development of the model.

2.1. Standard k-ω model in near wall regions

The hybrid turbulence model uses the standard k-ω formula in the near wall regions. The standard k-ω model solves two transport equations for turbulence kinetic energy (k) and specific dissipation rate (ω). The turbulence kinetic energy, k, is calculated by:

$$\frac{\partial}{\partial t}(\rho k) + \frac{\partial}{\partial x_i}(\rho k U_i) = \frac{\partial}{\partial x_j}\left(\Gamma_{k1}\frac{\partial k}{\partial x_j}\right) + G_{k1} - Y_{k1} \tag{1}$$

where t is the time, ρ the air density, U the Reynolds-averaged air velocity, x the coordinate, μ the air viscosity, μ_t the eddy viscosity, Γ_{k1} the effective diffusivity of k, G_{k1} the generation of k due to mean velocity gradients, and Y_{k1} the dissipation of k due to turbulence. The specific dissipation rate, ω_1, is calculated by:

$$\frac{\partial}{\partial t}(\rho \omega) + \frac{\partial}{\partial x_i}(\rho \omega U_i) = \frac{\partial}{\partial x_j}\left(\Gamma_{\omega 1}\frac{\partial \omega}{\partial x_j}\right) + G_{\omega 1} - Y_{\omega 1} \tag{2}$$

where $\Gamma_{\omega 1}$ is the effective diffusivity of ω, $G_{\omega 1}$ the generation of ω, and Y_{k1} the dissipation of ω due to turbulence. The detailed formulation of Γ_{k1}, G_{k1}, Y_{k1}, $\Gamma_{\omega 1}$, $G_{\omega 1}$, Y_{k1}, and the constants can be found in Wilcox [15].

2.2. Transformed RNG k-ε model in bulk air regions

The hybrid turbulence model utilizes the RNG k-ε formula in the bulk air regions. In the RNG k-ε model, a transport equation for the turbulence dissipation rate (ε) is used instead of ω. The RNG k-ε model calculates the turbulence kinetic energy, k, as follows:

$$\frac{\partial}{\partial t}(\rho k) + \frac{\partial}{\partial x_i}(\rho k U_i) = \frac{\partial}{\partial x_j}\left(\Gamma_{k2}\frac{\partial k}{\partial x_j}\right) + G_{k2} + G_b - \rho \varepsilon - Y_M \tag{3}$$

where Γ_{k2} is the effective diffusivity of k; G_{k2} and G_b the generation of k due to mean velocity gradients and buoyancy, respectively; and Y_M the contribution of the fluctuating dilatation in compressible turbulence to the overall dissipation rate. The dissipation rate, ε, is calculated by:

$$\frac{\partial}{\partial t}(\rho \varepsilon) + \frac{\partial}{\partial x_i}(\rho \varepsilon U_i) = \frac{\partial}{\partial x_j}\left(\Gamma_{\varepsilon 2}\frac{\partial \varepsilon}{\partial x_j}\right) + C_{1\varepsilon}\frac{\varepsilon}{k}(G_{k2} + C_{3\varepsilon}G_b) - C_{2\varepsilon}^*\rho\frac{\varepsilon^2}{k} \tag{4}$$

where $\Gamma_{\varepsilon 2}$ is the effective diffusivity of ε, and $C_{1\varepsilon}$, $C_{2\varepsilon}^*$, and $C_{3\varepsilon}$ are constants. The detailed formulation of Γ_{k2}, G_{k2}, G_b, $\Gamma_{\varepsilon 2}$, Y_M, and the constants can be found in Yakhot and Orszag [16].

To consolidate the standard k-ω model and the RNG k-ε model, one should transform the original RNG k-ε model into the same format as that of the standard k-ω model. The relationship between ε and ω can be expressed by:

$$\varepsilon = \beta^* \omega k \tag{5}$$

where β^* is a constant. When Eq. (5) is inserted into Eq. (3), the k equation becomes:

$$\frac{\partial}{\partial t}(\rho k) + \frac{\partial}{\partial x_i}(\rho k U_i) = \frac{\partial}{\partial x_j}\left(\Gamma_{k2}\frac{\partial k}{\partial x_j}\right) + G_{k2} + G_b - \rho\beta^*\omega k - Y_M \tag{6}$$

Next inserting Eq. (5) into Eq. (4) and performing a long derivation transforms the ε equation, Eq. (4), into the following:

$$\frac{\partial}{\partial t}(\rho\omega) + \frac{\partial}{\partial x_i}(\rho\omega U_i) = \frac{\partial}{\partial x_j}\left(\Gamma_{\omega 2}\frac{\partial\omega}{\partial x_j}\right) + 2\frac{\Gamma_{\omega 2}}{k}\frac{\partial k}{\partial x_j}\frac{\partial\omega}{\partial x_j}$$
$$+ (C_{1\varepsilon} - 1)\frac{\omega}{k}G_k - \left(C_{2\varepsilon}^* - 1\right)\rho\beta^*\omega^2 - \frac{\omega}{k}G_b + \frac{\omega}{k}Y_M \tag{7}$$

where $\Gamma_{\omega 2}$ is equal to $\Gamma_{\varepsilon 2}$. Eq. (7) is equivalent to Eq. (4) but has the same format as Eq. (2).

2.3. Hybrid turbulence model with blending functions

The hybrid turbulence model utilizes the standard k-ω model in the near wall regions and the transformed RNG k-ε model in the bulk air regions. This study employed a blending method to gradually switch the two models on and off. This blending method was proposed by Menter [17] and has been successfully applied to the SST k-ω model. When the standard k-ω model and transformed RNG k-ε model are combined, the equation for turbulence kinetic energy, k, in the hybrid turbulence model can be expressed by:

$$\frac{\partial}{\partial t}(\rho k) + \frac{\partial}{\partial x_i}(\rho k U_i) = \frac{\partial}{\partial x_j}\left(\Gamma_k\frac{\partial k}{\partial x_j}\right) + F_1(G_{k1} - Y_{k1})$$
$$+ (1 - F_1)\left(G_{k2} + G_b - \rho\beta^*\omega k - Y_M\right) \tag{8}$$

where Γ_k is the effective diffusivity of k, which can be calculated by:

$$\Gamma_k = F_1\Gamma_{k1} + (1 - F_1)\Gamma_{k2} \tag{9}$$

where F_1 is the blending function proposed by Menter [17], which is a function of the distance from the centroid of the cell to the nearest wall surface.

Using the same blending method, the equation for the specific dissipation rate, ω, in the hybrid turbulence model can be expressed by:

$$\frac{\partial}{\partial t}(\rho\omega) + \frac{\partial}{\partial x_i}(\rho\omega U_i) = \frac{\partial}{\partial x_j}\left(\Gamma_\omega\frac{\partial\omega}{\partial x_j}\right) + F_1(G_{\omega 1} - Y_{\omega 1})$$
$$+ (1 - F_1)\left[2\frac{\Gamma_{\omega 2}}{k}\frac{\partial k}{\partial x_j}\frac{\partial\omega}{\partial x_j} + (C_{1\varepsilon} - 1)\frac{\omega}{k}G_k \right. \tag{10}$$
$$\left. - \left(C_{2\varepsilon}^* - 1\right)\rho\beta^*\omega^2 - \frac{\omega}{k}G_b + \frac{\omega}{k}Y_M\right]$$

where Γ_ω is the effective diffusivity of ω, which can be calculated by:

$$\Gamma_\omega = F_1\Gamma_{\omega 1} + (1 - F_1)\Gamma_{\omega 2} \tag{11}$$

Note that the blending function, F_1, ranges from 0 to 1. When the cell is located next to a wall surface, F_1 is equal to 1 and the hybrid turbulence model is essentially the standard k-ω model. When the cell is far away from the wall, F_1 is equal to 0 and the hybrid turbulence model is equivalent to the RNG k-ε model. The blending function ensures that the hybrid model gradually changes from the standard k-ω model in the near wall regions to the RNG k-ε model in the bulk air regions. The detailed formulation of the blending function can be found in Menter [17]. The present study implemented a user-defined function code in ANSYS Fluent [18] to realize the proposed hybrid turbulence model.

In this study, the SIMPLE algorithm was employed as pressure-velocity coupling. The PRESTO! scheme was used for discretizing pressure and the second-order upwind scheme as discretion scheme for all the other variables. The averaged y^+ was around 5. The turbulence intensity at the supplies was set to be 10%, and the turbulence length scale was set to be the width of the supplies.

2.4. Contaminant transport and risk assessment

In addition to development of the turbulence model, the contaminant transport and infection risk should also be calculated. This study used the Eulerian model to calculate the contaminant transport in the aircraft cabins:

$$\frac{\partial\phi}{\partial t} + \frac{\partial}{\partial x_i}(\rho\phi U_i) = \frac{\partial}{\partial x_j}\left(\Gamma_\phi\frac{\partial\phi}{\partial x_j}\right) + S_\phi \tag{12}$$

where ϕ is the contaminant concentration, Γ_ϕ the diffusion coefficient, and S_ϕ the mass flow rate of source per unit volume. It was assumed that the infectious particles were sufficiently fine to follow the air movement [19]. On the basis of the calculated contaminant concentration in the breathing zone of each passenger, the risk of acquiring SARS during a flight was estimated using the Wells-Riley equation:

$$P_i = 1 - \exp\left(-C_{q,i}pt\right) \tag{13}$$

where $C_{q,i}$ is the concentration in the breathing zone of a passenger, calculated using the Eulerian method by setting the source equal to

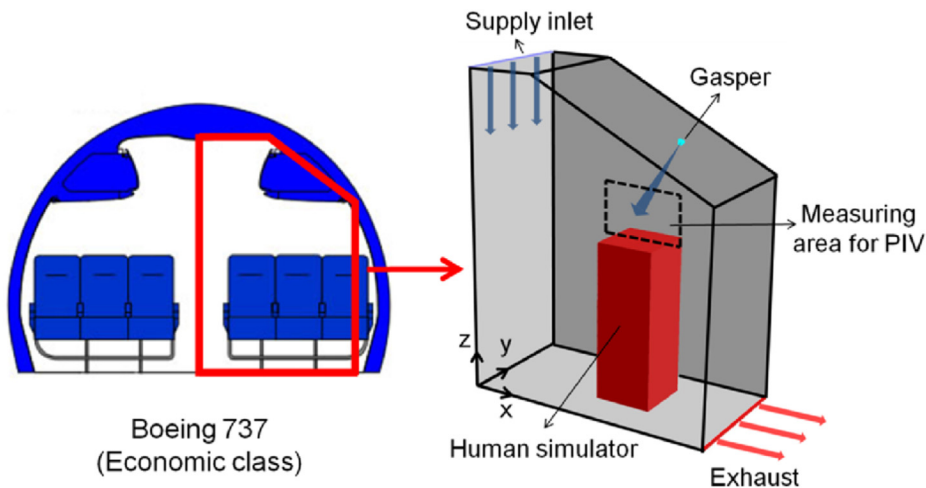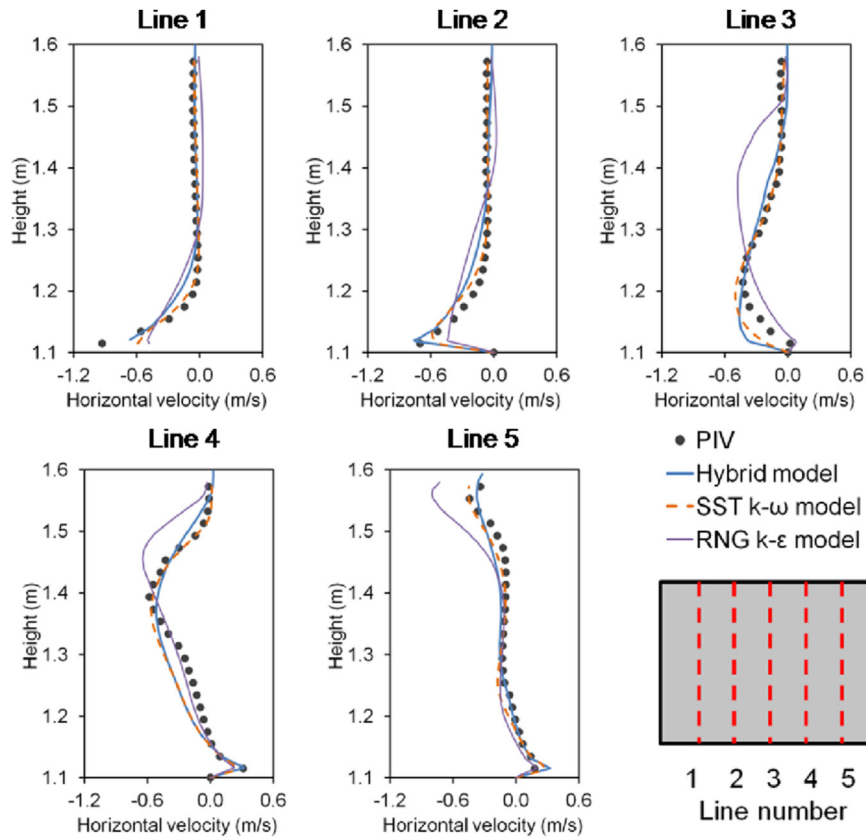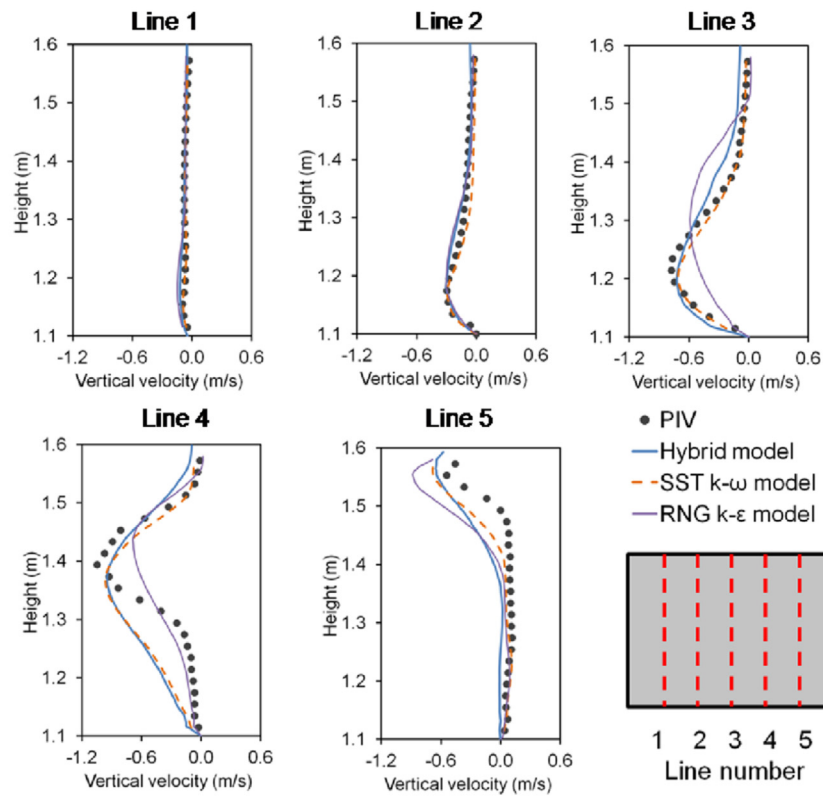

Fig. 1. Configuration of the aircraft cabin mock-up with gasper on [6].

(a)

(b)

Fig. 2. Comparison of the predicted and measured velocity profiles in (a) the horizontal and (b) the vertical direction in the measuring area.
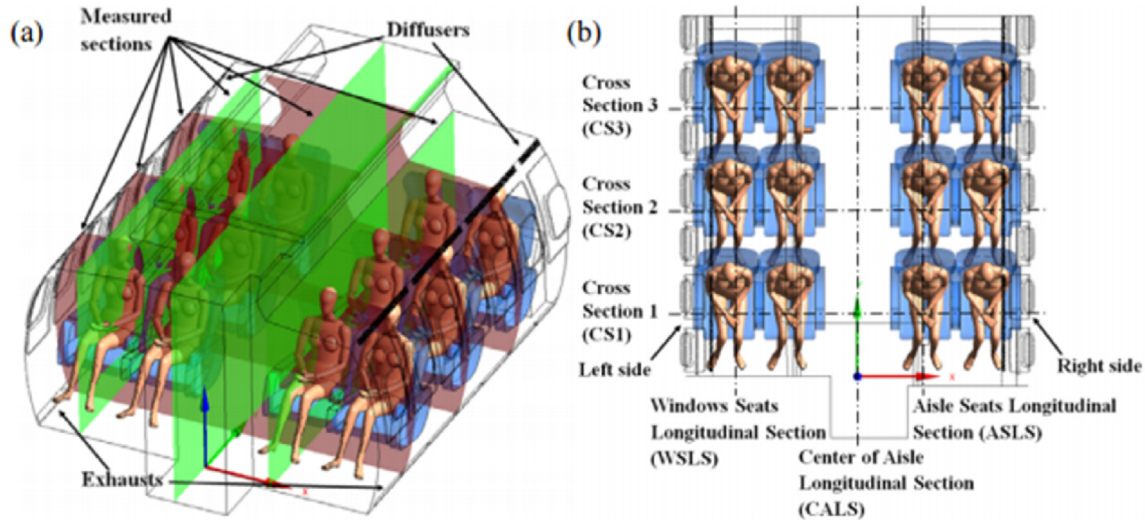
Fig. 3. Schematic of the fully occupied, first-class cabin and measured sections: (a) perspective view and (b) plane view [14].

the quanta of SARS; p is the breathing flow rate of each passenger; and t is the flight duration. Note that the index passenger was assumed to exhale virus continuously during the flight. Therefore, the potential infectious period of other passengers was the flight duration.

3. Model validation

This study used experimental data from two cases to validate the hybrid turbulence model. The first case was the airflow in a mock-up of half of a full-scale, one-row, single-aisle aircraft cabin with one gasper turned on, from You et al. [6]. This case was selected because the airflow measurement was accurate and had a high resolution. The second case was the airflow in the fully occupied first-class cabin of a real MD-82 commercial airliner from Liu et al. [14]. The present study used the second case in order to validate the model in a realistic scenario. This section details the validation of the model.

3.1. Mock-up of an aircraft cabin with gasper on

The first case was the airflow in a half-row cabin mock-up that simulated a Boeing 737 with one gasper turned on, from You et al. [6], as shown in Fig. 1. The dimensions of the mock-up were 1.75 m in width (x), 0.9 m in depth (y), and 2.2 m in height (z). A linear diffuser was installed on the aisle ceiling and supplied the main airflow, while the exhaust was located on the right-side wall at floor level. The supply-air velocity was 1.44 m/s. Additional air with a flow rate of 1.2 l/s was supplied through a gasper installed on the inclined surface of the ceiling. The total air change rate of the cabin mock-up was 33.5 ACH. A heated human simulator with a sensible heat load of 75 W was placed in the mock-up. You et al. [6] measured the two-dimensional airflow field in an area above the simulator, as identified in Fig. 1, using a particle image velocimetry (PIV) system. The high resolution of the measurement (512 × 384 data points) was useful for carefully validating the proposed hybrid model.

This study used the simplified gasper model proposed by You et al. [7] in the CFD simulation. Three grid resolutions, 0.2, 0.3, and 0.65 million, were tested in You et al. [7] for CFD grid independence. The resolution of 0.3 million was sufficiently fine to obtain grid independent results. Fig. 2 compares the predicted velocity profiles

from the hybrid turbulence model with the measured data. The horizontal velocity profiles at five lines in the measuring area are shown in Fig. 2(a), while the vertical velocity profiles are shown in Fig. 2(b). In addition to the results from the hybrid turbulence model, the figure displays the results from the RNG k-ε model and the SST k-ω model. In both the horizontal and vertical directions, the velocity profiles predicted by the hybrid model and the SST k-ω model agreed very well with the experimental data. However, the agreement between the results from the RNG k-ε model and the measured data was unsatisfactory. The RNG k-ε model failed to capture the peaks in the horizontal direction, and failed to accurately predict the velocity profile in the vertical direction, especially at lines 3, 4, and 5.

To quantitatively compare the accuracy of the models, the normalized root mean square errors (NRMSE) between the predicted and measured data were calculated by:

$$NRMSE = \frac{\sqrt{\left[\sum_{i=1}^{n} \left(\phi_{\exp,i} - \phi_{\text{model},i}\right)^2\right] \Big/ n}}{\phi_{\exp,\max} - \phi_{\exp,\min}} \tag{14}$$

where $\phi_{\exp,i}$ is a data point from the experimental data, $\phi_{\text{model},i}$ is the corresponding data point from the CFD simulation, and $\phi_{\exp,\max}$ and $\phi_{\exp,\min}$ are the maximum and minimum values, respectively, of the experimental data. For the horizontal velocity profile, the overall NRMSE of the hybrid turbulence model, the SST k-ω model, and the RNG k-ε model were 0.076, 0.065, and 0.155, respectively. For the vertical velocity profile, the overall NRMSE were 0.123, 0.107, and 0.139, respectively. For both horizontal and vertical profiles, the performance of the hybrid turbulence model was slightly worse than that of the SST k-ω model, but better than that of the RNG k-ε model. This case verified the superiority of the hybrid turbulence model in predicting the interaction of the gasper-induced jet flow with the thermal plume from the human body, when compared with the RNG k-ε model.

3.2. First-class cabin of a real MD-82 airliner

The second case was the airflow in the fully occupied first-class cabin of a functional MD-82 commercial airliner from Liu et al. [14], as shown in Fig. 3. There were three rows of seats, with four seats in

RNG k-ε model   SST k-ω model

Hybrid model

(a)

RNG k-ε model   SST k-ω model

Hybrid model

(b)
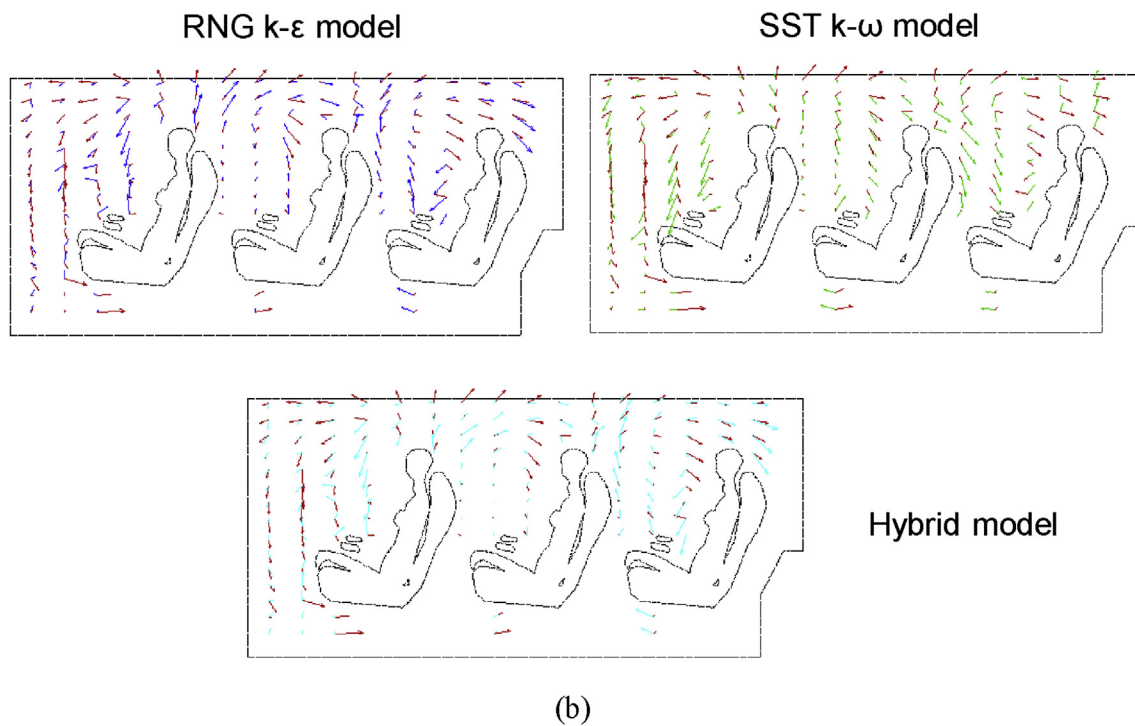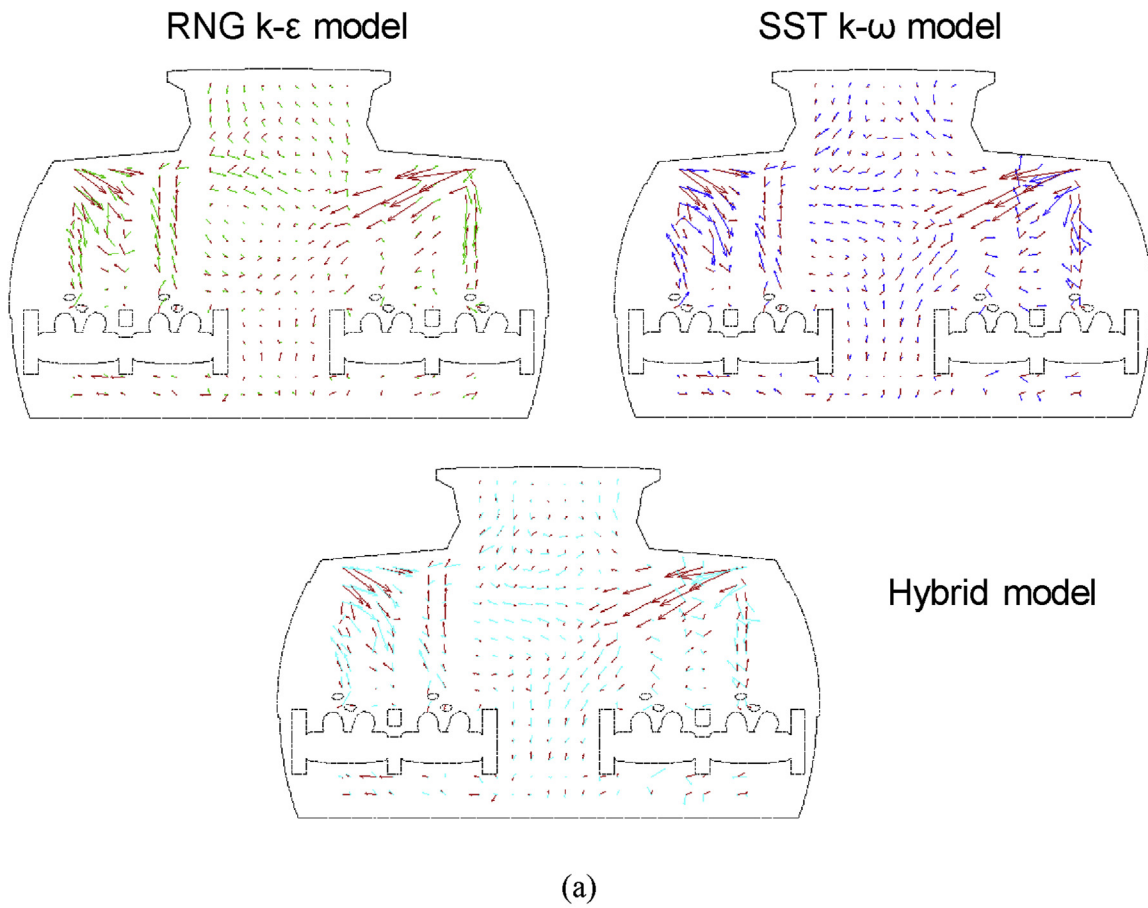
Fig. 4. Comparison of the computed and measured airflow patterns in (a) CS3 and (b) ASLS in the fully occupied cabin.

(a)

(b)
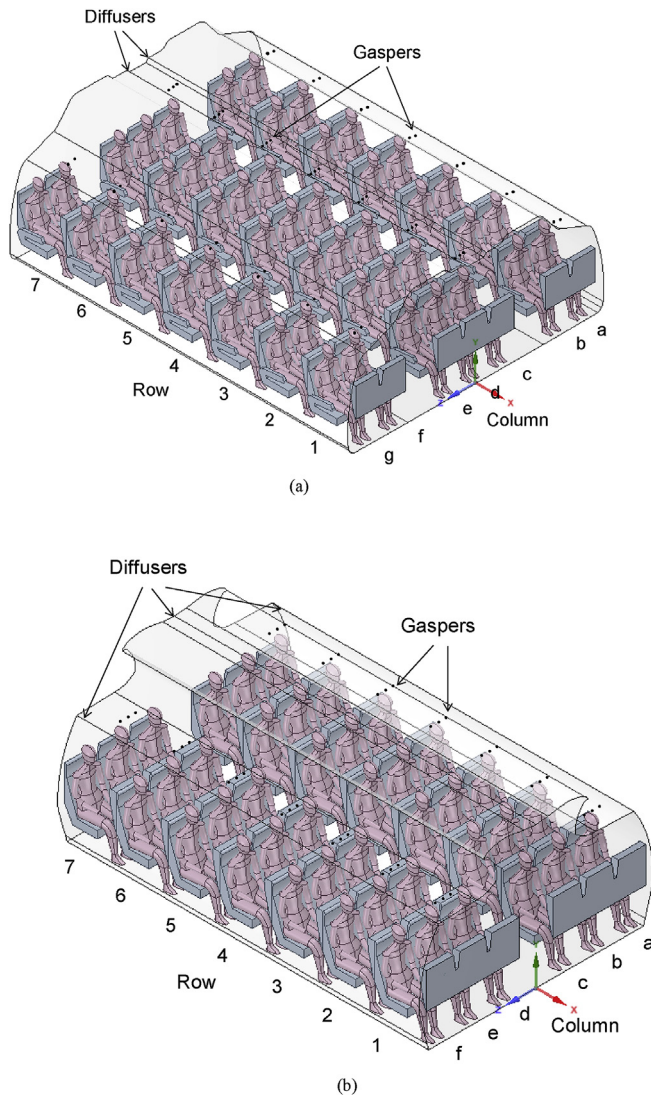
Fig. 5. Schematic of the seven-row section of fully occupied, economy-class cabin of (a) the Boeing 767 and (b) the Boeing 737. The black dots at the ceiling represent the gaspers, the sizes of which are very small compared with the cabin.

each row. Heated manikins were used to simulate the passengers, with a sensible heat production of 75 W for each manikin. The total air change rate was 33 ACH. The three-dimensional airflow fields were measured with ultrasonic anemometers in three cross sections and three longitudinal sections in the cabin, as shown in Fig. 3. This real airplane case was selected for validation of the model under a realistic scenario.

Liu et al. [14] tested three grid resolutions (6.4, 8.4, and 13 million) and found that a resolution of 6.4 million grid was sufficiently fine to capture the airflow in the cabin. This study compared the calculated flow field from the hybrid turbulence model with the measured data at all the sections. The results predicted from the RNG k-ε model and the SST k-ω model were also included in the comparison. To keep the paper concise, only the comparisons of the airflow vectors at sections Cross Section 3 (CS3) and Aisle Seats Longitudinal Section (ASLS) are shown in Fig. 4. It can be seen that all three turbulence models were able to predict the general trends of the airflow distributions reasonably well. The results at the other sections led to the same conclusion.

To quantitatively compare the accuracy of the models, the

NRMSE of different turbulence models were calculated and compared. The overall NRMSE of the hybrid turbulence model (0.138) was slightly lower than that of the SST k-ω model (0.141), but slightly greater than that of the RNG k-ε model (0.129). Note that the measurements were taken in the bulk air regions. In these regions, the hybrid turbulence model is expected to be robust because it utilizes the RNG k-ε model. This case, with measured data in a real aircraft cabin, shows that the hybrid model can be successfully applied in a realistic and complex scenario.

In summary, the first case, with accurate and high-resolution data, confirmed that the hybrid turbulence model was superior to the RNG k-ε model, especially in the near wall regions. The second case, with measured data in a real airplane, demonstrated that the hybrid model could be successfully applied in realistic and complex cases. Therefore, the developed hybrid turbulence model was used to investigate the impact of gaspers on cabin air quality in commercial airliners, as discussed in the next section.

4. Impact of gaspers on cabin air quality

The investigation aimed to determine whether turning on the gaspers would enhance the cabin air quality in commercial airliners. The validated hybrid turbulence model was used to calculate the air distribution, contaminant transport, and risk of infection by SARS in the economy-class cabins of the two most widely-used airplanes, Boeing 767 and Boeing 737, under different gasper on/off distributions.

4.1. Case setup

Fig. 5(a) and (b) are schematics of the seven-row section of fully occupied economy-class cabin of Boeing 767 and Boeing 737 airplanes, respectively, with the seat numbers marked. The Boeing 767 has a twin-aisle cabin with seven seats in each row. Two supply-air diffusers are located in the center of the ceiling, and the exhausts are installed in the side walls near the floor. For passengers seated on the outside of the two aisles (seats a, b, f and g), individual gaspers is installed in the ceiling above the seats to provide fresh air. For the passengers seated between the aisles (seats c, d, and e), gaspers are installed in the middle of the ceiling. In contrast, the Boeing 737 has a single-aisle cabin with six seats in each row. Two main supply-air diffusers are located in the center of the ceiling and another two side diffusers in the ceiling above the window seats. The exhausts are installed in the side walls near the floor. The gaspers are installed in the ceiling, one above each passenger. The total ventilation rate was set at 33.7 ACH for both airplanes [20]. The airflow rate from each gasper was set at 0.66 L/s [8]. The supply-air temperature was 19.3 °C. The temperatures of the walls and the passengers were set at 24.5 and 31 °C, respectively. According to symmetry, this study evaluated four source locations, the mouths of passengers seated at d4, e4, f4, and g4, in the Boeing 767. Similarly, three source locations, the mouths of passengers seated at c4, d4, and e4, were considered in the Boeing 737.

Each passenger may choose whether or not to turn on his/her gasper. Thus, there are billions of possible gasper on/off distributions in the cabin. Calculating all the possible scenarios was unrealistic. Therefore, the quasi-random sampling method [21] was adopted to determine representative gasper on/off distributions. To illustrate the method, this paper uses the Boeing 767 cases as an example. First, this study considered five different gasper on/off ratios, 0%, 25%, 50%, 75%, and 100%. These ratios indicate that, of the total of 49 gaspers, the corresponding number of gaspers that are turned on is 0, 12, 24, 37, or 49, respectively. For each gasper on/off ratio, there are still billions of possible distributions. For instance, when the gasper on/off ratio is 25%, 12 out of 49 gaspers are turned

(a)

(b)
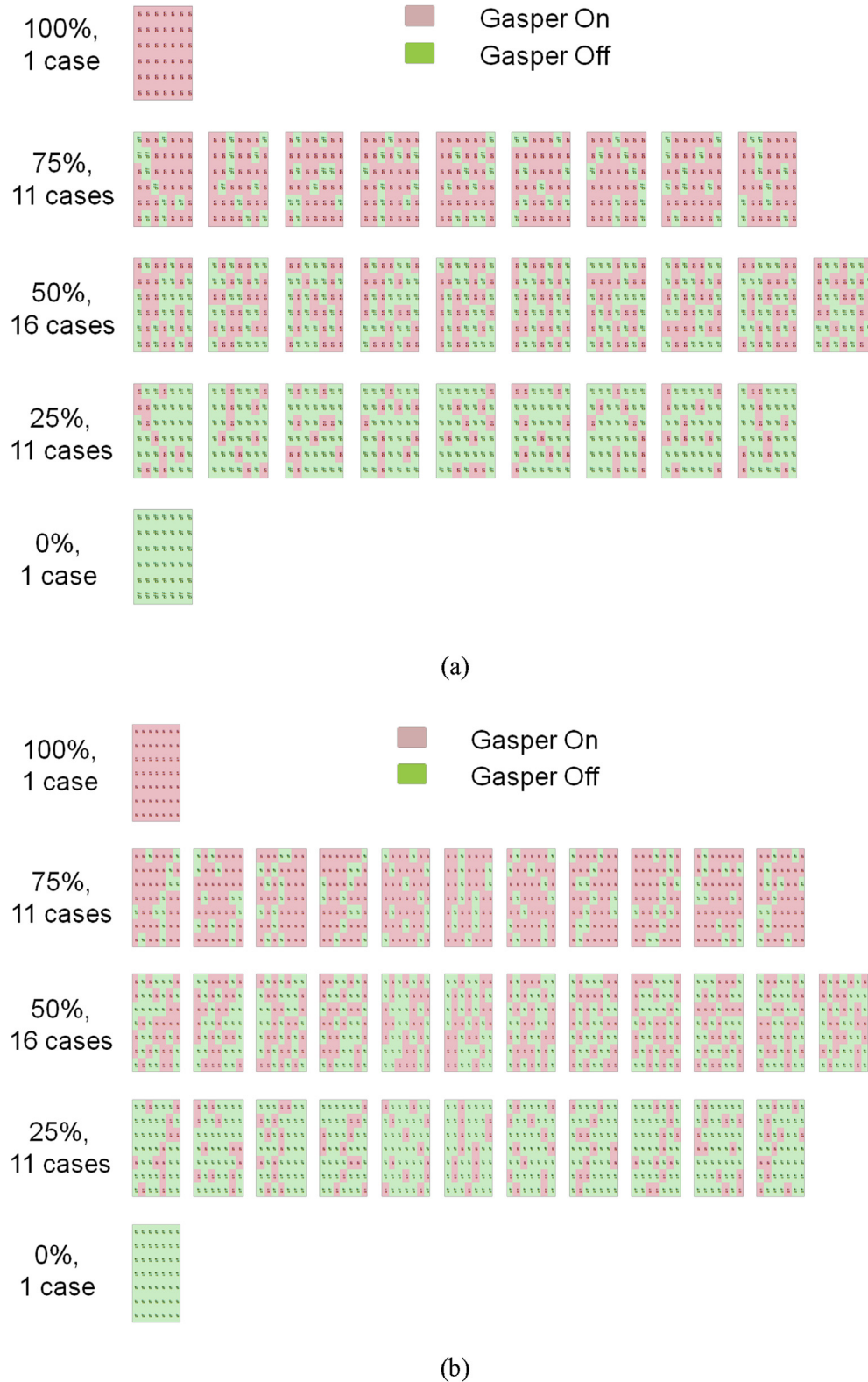
Fig. 6. Gasper on/off distributions determined using the quasi-random sampling method for (a) the Boeing 767 and (b) the Boeing 737.

on. Therefore, there are $C_{49}^{12} = 9.2 \times 10^{10}$ possible scenarios. To reduce the number of cases, this investigation performed a quasi-random sampling. First, the gaspers corresponding to the seats from a1 to g7 were numbered from 1 to 49. Next, twelve numbers were quasi-randomly selected from the 49 using a Matlab code.

Each quasi-random process corresponded to a specific gasper on/off distribution. Note that in this case, when the number of runs of the quasi-random process is sufficiently large, the chance of turning on the gasper for each passenger converges to 25%. In other words, the generated cases are representative of all the gasper on/off
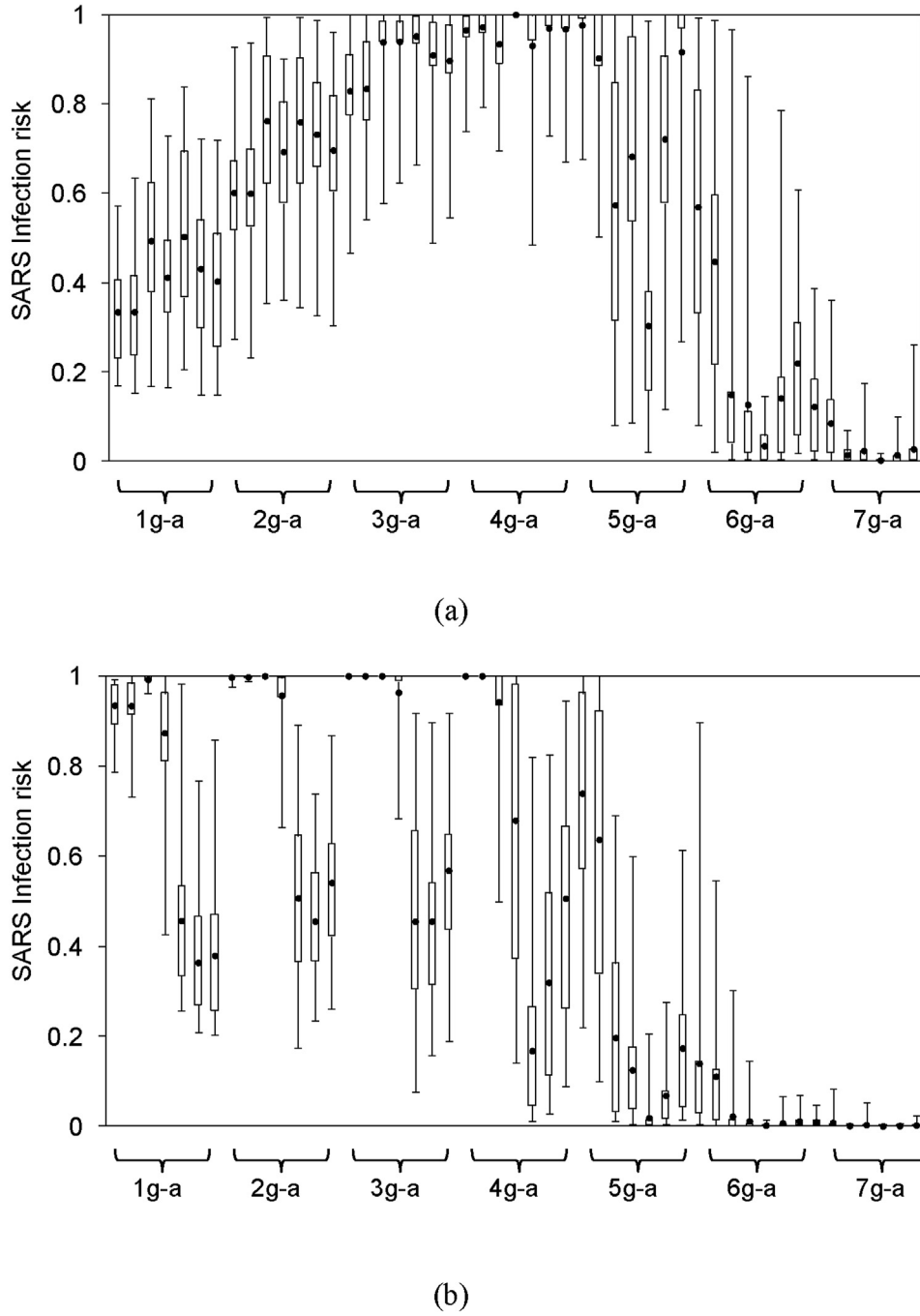
(a)

(b)

Fig. 7. SARS infection risk distribution for each passenger in the database with the source at seats (a) 4d and (b) 4g in the Boeing 767.

distributions when the gasper on/off ratio is 25%. To obtain the representative cases with a reasonable tolerance of error, one should determine how many runs of the quasi-random process are needed.

This study calculated the normalized root mean square error (NRMSE) of the chance of turning on the gasper for each passenger under different numbers of runs by:

$$NRMSE = \frac{\sum_{i=1}^{n} \sqrt{\frac{(x_i - \bar{x})^2}{n}}}{x_{\max} - x_{\min}} \tag{15}$$

where n is the total number of passengers, x_i is the chance of

turning on the gasper for a passenger under a given number of runs, $\bar{x}$ is the expectancy of the chance of turning on the gasper for a passenger, $x_{\max}$ is 100%, and $x_{\min}$ is 0%. Still using the gasper on/off ratio of 25% for the Boeing 767 as an example, then, n is 49 and $\bar{x}$ is 25%. This investigation set the tolerance of error at 10%. Thus, when the calculated NRMSE under a given number of runs was less than 10%, the generated cases were representative of all the gasper on/off distributions. Using this criterion, the total numbers of cases under different gasper on/off ratios could be determined. Fig. 6 shows the detailed gasper on/off distributions for the Boeing 767 and Boeing 737 obtained from the quasi-random sampling method. The total number of gasper on/off distribution scenarios is 30 for
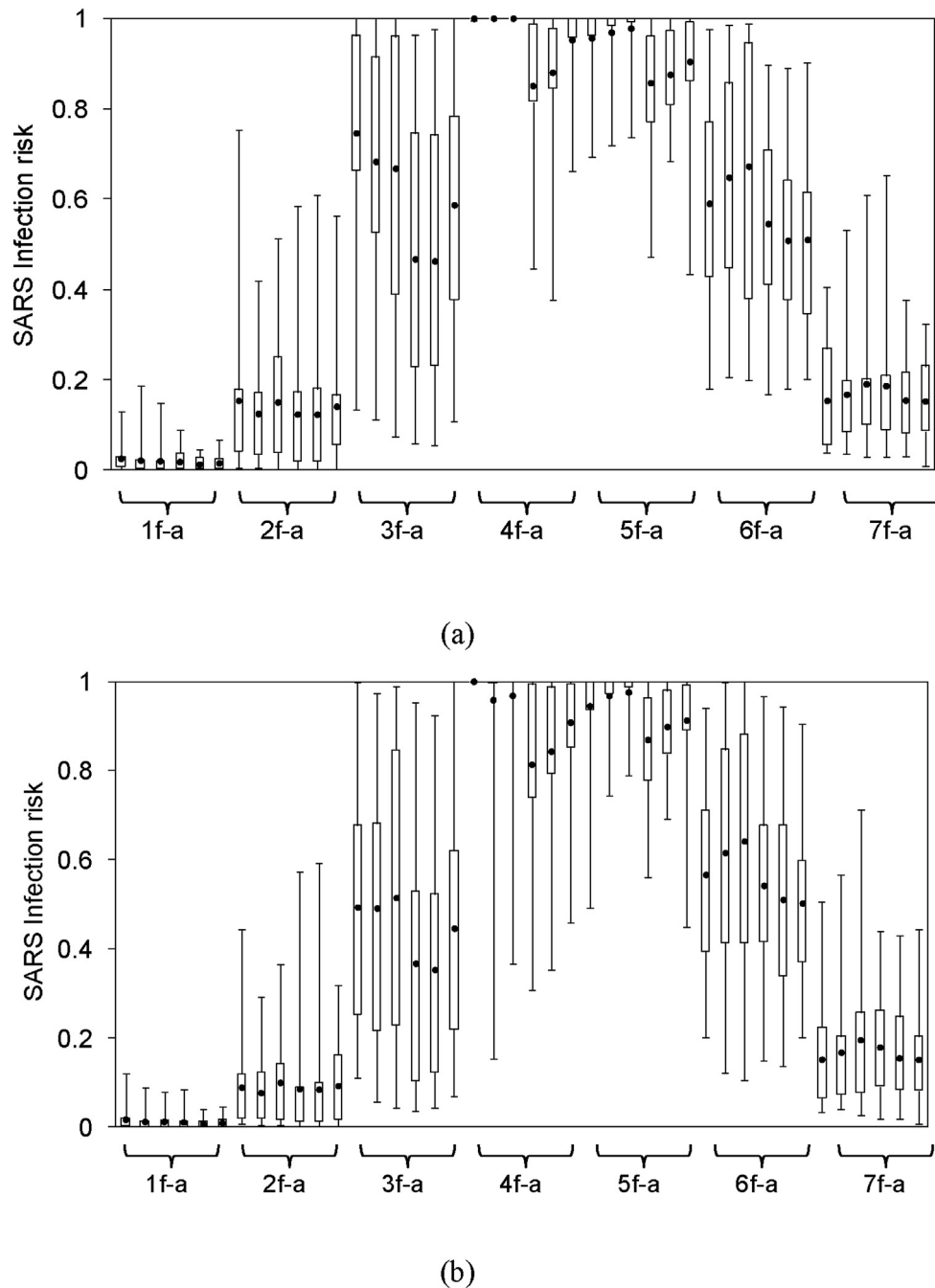
(a)

(b)

Fig. 8. SARS infection risk distribution for each passenger in the database with the source at seats (a) 4d and (b) 4f in the Boeing 737.

each airplane.

The validated hybrid turbulence model was then used to calculate the airflow distribution with the gasper on/off distributions determined by the quasi-random sampling method. The contaminant concentration distribution for each case was calculated using the Eulerian method. Finally, the risk of acquiring SARS for each passenger was calculated using the Wells-Riley equation. The quanta of SARS was set at 2670 per hour [22], and the breathing flow rate of each passenger was set at 0.00053 m³/s, according to the ISO standard [23]. The flight durations for the Boeing 767 and Boeing 737 were set at 5 and 2 h, respectively, according to the actual durations of 1000 flights of the major airliners in the U.S. Since there were four contaminant source locations in the Boeing

767 and three locations in the Boeing 737, the total number of CFD cases was 420. Furthermore, there were 49 passengers in the cabin of the Boeing 767 and 42 in the Boeing 737; thus, this study generated a database containing 9660 data points for the risk of acquiring SARS.

4.2. Results and discussion

The infection risk of SARS for a given passenger would be different under different gasper on/off distributions and with different source locations. In other words, for a given source location, the database contains many data points for each passenger, corresponding to different gasper on/off distributions. Using the
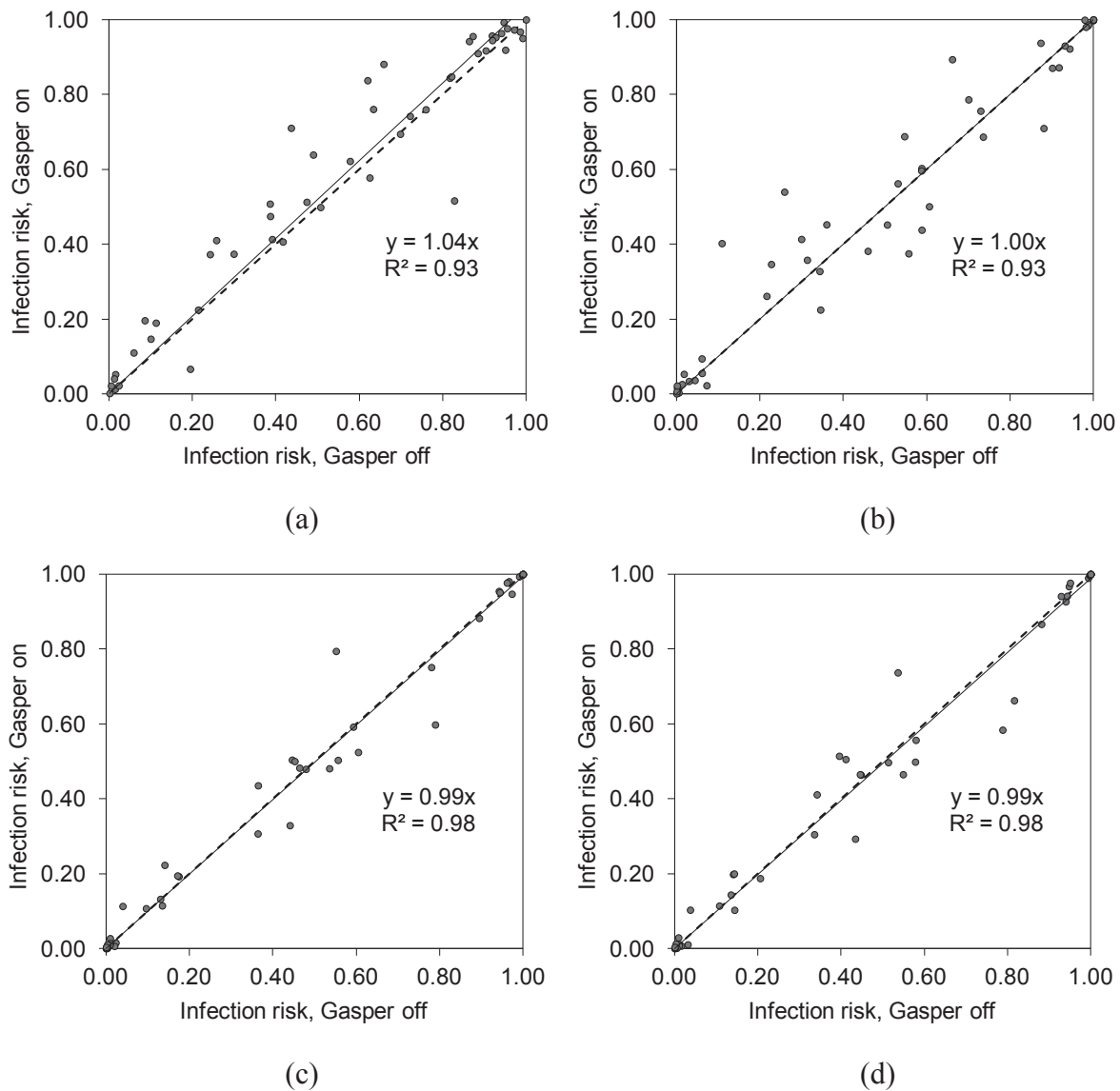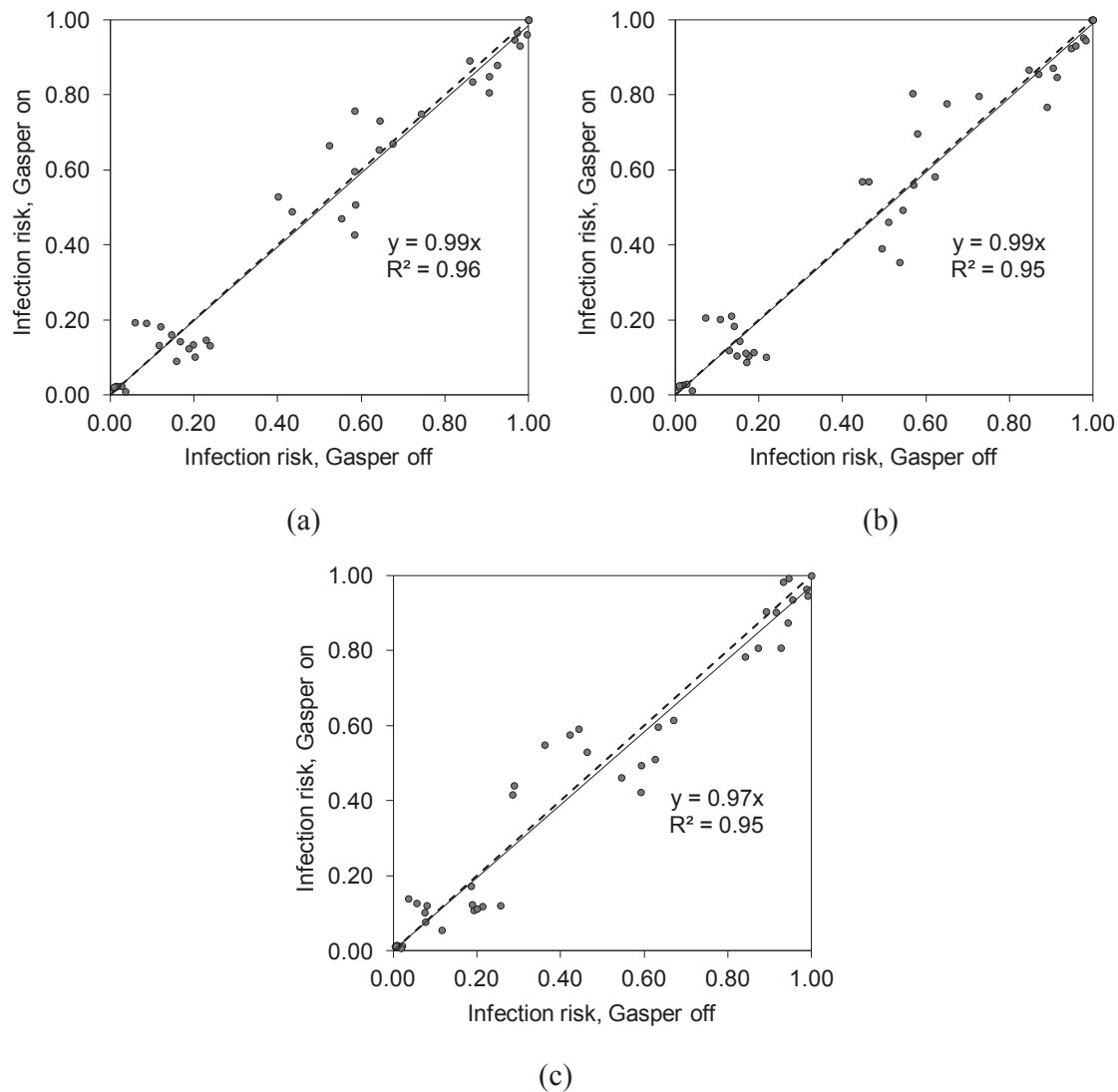
Fig. 9. Comparison of SARS infection risk when the gasper was turned on and off for each passenger in the Boeing 767 with the source location at seats (a) 4d, (b) 4e, (c) 4f, and (d) 4g.

database, this study calculated the mean, maximum, minimum, 75th percentile, and 25th percentile of the infection risks for each passenger with various source locations. Fig. 7(a) and (b) show the data for each passenger when the source was located at seats 4d and 4g, respectively, in the Boeing 767. The points, the upper and lower bounds of the error bars, and the upper and lower bounds of the boxes represent the mean, the maximum and minimum, and the 75th and 25th percentiles, respectively, of the infection risks for each passenger. Note that these variations were caused by the different gasper on/off distributions. The results show that the gasper on/off distribution can significantly affect the infection risk for each passenger. For example, when the source was at 4g, the SARS infection risk for the passenger seated at 3c ranged from 0.08 to 0.92 under different distributions. This variation occurred because the gasper-induced flows altered the air distribution in the cabin, which in turn influenced contaminant transport from the source and the receptors. To keep the paper concise, only the results with the source at seats 4d and 4g are shown in the figure. The results with the source at seats 4e and 4f point to the same

conclusion.

Fig. 8 shows the results for the Boeing 737. This figure is analogous to Fig. 7, except that the source in the Boeing 737 was at seats 4d and 4f. As in the Boeing 767, the SARS infection risk can be significantly influenced by the gasper on/off distribution. For instance, when the source was at 4d, the infection risk for the passenger seated at 6f ranged from 0.18 to 0.98 under different distributions. Therefore, for both the Boeing 767 and Boeing 737, the impact of gaspers on cabin air quality was significant.

Figs. 7 and 8 show that turning on the gaspers may significantly affect the infection risk for each passenger. Statistically speaking, however, it is still unknown whether turning on a passenger's gasper will have a positive or negative impact on his/her infection risk. To answer this question, this study calculated the mean infection risk from the database for each passenger when he/she turned on his/her gasper. The mean infection risk for each passenger when he/she did not turn on the gasper was also calculated. Note that Figs. 9 and 10 included all cases in the database. Fig. 9 compares the mean SARS infection risk for the 49 passengers in

(a)

(b)

(c)

Fig. 10. Comparison of SARS infection risk when the gasper was turned on and off for each passenger in the Boeing 737 with the source location at seats (a) 4c, (b) 4d, and (c) 4e.

the Boeing 767 when they turned their gaspers on and off. The horizontal axis indicates the mean infection risk when the gasper was off, while the vertical axis indicates the risk when the gasper was on. The solid line represents the 1:1 line, while the dashed line is the linear regression. Each point represents a passenger. If a point is located exactly on the 1:1 line, it means that there was no difference in the mean infection risk for that passenger when his/her gasper was turned on and off. If a point is above the 1:1 line, it means that turning on the gasper increased the mean infection risk for this passenger. If a point is below the 1:1 line, the risk was reduced by turning the gasper on. It can be seen in the figures that most of the points are close to the 1:1 line, and the slopes of the linear regressions are close to 1 with high R^2 values. These results indicate that, statistically speaking, the overall effect of turning on a passenger's gasper on the mean infection risk for the passenger was neutral for the general population.

Fig. 10 is analogous to Fig. 9, except that there were 42 passengers in the Boeing 737. Again, most of the points were close to the 1:1 line, and the slopes of the linear regressions were close to 1 with high R^2 values. The results for the Boeing 737 led to the same conclusion as for the 767: statistically speaking, if a passenger turned on his/her gasper, there was an equal chance of either a positive or negative impact on his/her infection risk.

There are important practical implications of the results presented above. First, the gasper on/off distribution can significantly influence the infection risk for each passenger. Furthermore, statistically speaking, the overall effect of turning on a passenger's gasper on the mean infection risk for the passenger is neutral. That is to say, turning on a passenger's gasper could result in either a positive or negative impact on his/her infection risk. The practical implication is that, even though a gasper supplies clean air that is aimed at a passenger, it may actually have a negative effect on the passenger's health. If the specific gasper on/off distribution produces a high contaminant concentration in the region above a passenger's head, turning on the gasper may bring more contaminants into the breathing zone of the passenger as a result of the strong air entrainment [10]. Therefore, when a passenger is deciding whether or not to turn on his/her gasper, the conventional understanding that the clean air supplied from the gasper enhances the air quality is not necessarily correct. If the passenger's health is fragile, he/she should consider not turning on the gasper to avoid the possibility of increased infection risk.

5. Conclusions

This study aimed to answer the following question: if a passenger turns on his/her gasper in a commercial airliner, will his/her infection risk be reduced? First, this investigation developed a hybrid turbulence model for cabin airflow simulations and validated the model with two sets of experimental data. This study then used the validated model to numerically investigate the impact of gaspers on the cabin air quality in a seven-row section of economy-class cabin of a Boeing 767 and Boeing 737 airplanes. Within the scope of this study, the following conclusions can be made:

(1) The hybrid turbulence model that was developed is not only robust in the bulk air regions but also accurate in the near wall regions; furthermore, it can predict the air distribution in aircraft cabins reasonably well.
(2) The gasper on/off distribution can significantly influence the SARS infection risk for passengers in both the Boeing 767 and Boeing 737.
(3) Statistically speaking, the overall effect of turning on a passenger's gasper on the mean infection risk for the passenger is neutral.
(4) Even though a gasper supplies clean air that is aimed at the passenger, it may actually have a negative impact on the passenger's health.

Acknowledgements

References

[1] Y. Li, G.M. Leung, J.W. Tang, X. Yang, C.Y.H. Chao, J.Z. Lin, J.W. Lu, P.V. Nielsen, J. Niu, H. Qian, A.C. Sleigh, Role of ventilation in airborne transmission of infectious agents in the built environment—A multidisciplinary systematic review, Indoor Air 17 (1) (2007) 2—18.

[2] M.R. Moser, T.R. Bender, H.S. Margolis, G.R. Noble, A.P. Kendal, D.G. Ritter, An outbreak of influenza aboard a commercial airliner, Am. J. Epidemiol. 110 (1) (1979) 1—6.

[3] T.A. Kenyon, S.E. Valway, W.W. Ihle, I.M. Onorato, K.G. Castro, Transmission of multidrug-resistant Mycobacterium tuberculosis during a long airplane flight, N. Engl. J. Med. 334 (15) (1996) 933—938.

[4] S.J. Olsen, H.L. Chang, T.Y.Y. Cheung, A.F.Y. Tang, T.L. Fisk, S.P.L. Ooi, H.W. Kuo, D.D.S. Jiang, K.T. Chen, J. Lando, K.H. Hsu, Transmission of the severe acute respiratory syndrome on aircraft, N. Engl. J. Med. 349 (25) (2003) 2416—2422.

[5] ACI (Airports Council International), The Global Airport Community, 2007. www.airports.org/aci/aci/file/AnnualReport/ACIAnnualReport2006FINAL.pdf.

[6] R. You, J. Chen, Z. Shi, W. Liu, C.H. Lin, D. Wei, Q. Chen, Experimental and numerical study of airflow distribution in an aircraft cabin mock-up with a gasper on, J. Build. Perform. Simul. (2016), http://dx.doi.org/10.1080/19401493.2015.1126762.

[7] R. You, W. Liu, J. Chen, C.-H. Lin, D. Wei, Q. Chen, Predicting airflow distribution and contaminant transport in aircraft cabins with a simplified gasper model, J. Build. Perform. Simul. (2016) (in press).

[8] B. Li, R. Duan, J. Li, Y. Huang, H. Yin, C.H. Lin, D. Wei, X. Shen, J. Liu, Q. Chen, Experimental studies of thermal environment and contaminant transport in a commercial aircraft cabin with gaspers on, Indoor Air (2016), http://dx.doi.org/10.1111/ina.12265.

[9] S. Dai, H. Sun, W. Liu, Y. Guo, N. Jiang, J. Liu, Experimental study on characteristics of the jet flow from an aircraft gasper, Build. Environ. 93 (2015) 278—284.

[10] Z. Shi, J. Chen, R. You, C. Chen, Q. Chen, Modeling of gasper-induced jet flow and its impact on cabin air quality, Energy Build. 127 (2016) 700—713.

[11] Q. Chen, Comparison of different k-ε models for indoor air flow computations, Numer. Heat. Transf. Part B—Fundam. 28 (3) (1995) 353—369.

[12] Z. Zhang, W. Zhang, Z.J. Zhai, Q.Y. Chen, Evaluation of various turbulence models in predicting airflow and turbulence in enclosed environments by CFD: Part 2—comparison with experimental data from literature, HVAC&R Res. 13 (6) (2007) 871—886.

[13] M. Wang, Q. Chen, Assessment of various turbulence models for transitional flows in an enclosed environment (RP-1271), HVAC&R Res. 15 (6) (2009) 1099—1119.

[14] W. Liu, J. Wen, C.H. Lin, J. Liu, Z. Long, Q. Chen, Evaluation of various categories of turbulence models for predicting air distribution in an airliner cabin, Build. Environ. 65 (2013) 118—131.

[15] D.C. Wilcox, Reassessment of the scale-determining equation for advanced turbulence models, AIAA J. 26 (11) (1988) 1299—1310.

[16] V. Yakhot, S.A. Orszag, Renormalization group analysis of turbulence. I. Basic theory, J. Sci. Comput. 1 (1) (1986) 3—51.

[17] F.R. Menter, Two-equation eddy-viscosity turbulence models for engineering applications, AIAA J. 32 (8) (1994) 1598—1605.

[18] ANSYS, Fluent 12.1 Documentation, Fluent Inc., Lebanon, NH, 2010.

[19] C. Chen, W. Liu, C.H. Lin, Q. Chen, A Markov chain model for predicting transient particle transport in enclosed environments, Build. Environ. 90 (2015) 30—36.

[20] J.K. Gupta, C.-H. Lin, Q. Chen, Risk assessment for airborne infectious diseases in aircraft cabins, Indoor Air 22 (2012) 388—395.

[21] S.G. Nash, Quasi-random Sampling, in: Encyclopedia of Statistical Sciences, 1986.

[22] H. Qian, Y. Li, P.V. Nielsen, X. Huang, Spatial distribution of infection risk of SARS transmission in a hospital ward, Build. Environ. 44 (8) (2009) 1651—1658.

[23] ISO, Respiratory Protective Devices—Human Factors. Part 1. Metabolic Rates and Respiratory Flow Rates, ISO/TS, 16976—1, Geneva, 2007.